

Alleviating the Transit Timing Variations bias in transit surveys

II. RIVERS: Twin resonant Earth-sized planets around Kepler-1972 recovered from Kepler's false positive

A. Leleu¹, J.-B. Delisle¹, R. Mardling², S. Udry¹, G. Chatel³, Y. Alibert⁴ and P. Eggenberger¹

¹ Observatoire de Genève, Université de Genève, Chemin Pegasi, 51, 1290 Versoix, Switzerland.

² School of Physics and Astronomy, Monash University, Victoria 3800, Australia.

³ Disaitek, www.disaitek.ai.

⁴ Physikalisches Institut, Universität Bern, Gesellschaftsstr. 6, 3012 Bern, Switzerland.

January 28, 2022

ABSTRACT

Transit Timing Variations (TTVs) can provide useful information for systems observed by transit, by putting constraints on the masses and eccentricities of the observed planets, or even constrain the existence of non-transiting companions. However, TTVs can also prevent the detection of small planets in transit surveys, or bias the recovered planetary and transit parameters. Here we show that Kepler-1972 c, initially the "not transit-like" false positive KOI-3184.02, is an Earth-sized planet whose orbit is perturbed by Kepler-1972 b (initially KOI-3184.01). The pair is locked in a 3:2 Mean-motion resonance, each planet displaying TTVs of more than 6h hours of amplitude over the duration of the Kepler mission. The two planets have similar masses $m_b/m_c = 0.956_{-0.051}^{+0.056}$ and radii $R_b = 0.802_{-0.041}^{+0.042} R_{Earth}$, $R_c = 0.868_{-0.050}^{+0.051} R_{Earth}$, and the whole system, including the inner candidate KOI-3184.03, appear to be coplanar. Despite the faintness of the signals (SNR of 1.35 for each transit of Kepler-1972 b and 1.10 for Kepler-1972 c), we recovered the transits of the planets using the RIVERS method, based on the recognition of the tracks of planets in river diagrams using machine learning, and a photo-dynamic fit of the lightcurve. Recovering the correct ephemerides of the planets is essential to have a complete picture of the observed planetary systems. In particular, we show that in Kepler-1972, not taking into account planet-planet interactions yields an error of $\sim 30\%$ on the radii of planets b and c, in addition to generating in-transit scatter, which leads to mistake KOI3184.02 for a false positive. Alleviating this bias is essential for an unbiased view of Kepler systems, some of the TESS stars, and the upcoming PLATO mission.

Use \titlerunning to supply a shorter title and/or \authorrunning to supply a shorter list of authors.

1. Introduction

The most successful technique for detecting exoplanets - in terms of number of planets detected - is the transit method: when a planet passes in front of a star, the flux received from that star decreases. It has been, is, and will be applied by several space missions such as CoRoT, Kepler/K2, TESS, and the upcoming PLATO mission, to try and detect planets in large areas of the sky. When a single planet orbits a single star, its orbit is periodic, which implies that the transit happens at fixed time interval. This constraint is used to detect planets when their individual transits are too faint with respect to the noise of the data: using algorithms such as Boxed Least Squares (BLS, Kovács et al. 2002), the data reduction pipelines of the transit survey missions fold each lightcurve over a large number of different periods and look for transits in the folded data (Jenkins et al. 2010, 2016). This folding of the lightcurve increases the number of observation per phase, hence the signal-to-noise of the transit.

As soon as two or more planets orbit around the same star, their orbits cease to be strictly periodic. In some cases the gravitational interaction of planets can generate relatively short-term Transit Timing Variations (TTVs): transits do not occur at a fixed period any more (Dobrovolskis

& Borucki 1996; Agol et al. 2005). The amplitude, frequencies, and overall shape of these TTVs depend on the orbital parameters and masses of the planets involved (see for example Lithwick et al. 2012; Nesvorný & Vokrouhlický 2014; Agol & Deck 2016). As the planet-planet interactions that generate the TTVs typically occur on timescales longer than the orbital periods, space missions with longer baselines such as Kepler and PLATO are more likely to observe such effects. Since the end of the Kepler mission, several efforts have been made to estimate the TTVs of the Kepler Objects of Interest (KOIs) (Mazeh et al. 2013; Rowe & Thompson 2015; Holczer et al. 2016; Kane et al. 2019).

TTVs are a goldmine for our understanding of planetary systems: they can constrain the existence of non-transiting planet, hence adding missing pieces to the architecture of the systems (Xie et al. 2014; Zhu et al. 2018), allowing for a better comparison with synthetic planetary system population synthesis (see for example Mordasini et al. 2009; Alibert et al. 2013; Mordasini 2018; Coleman et al. 2019; Emsenhuber et al. 2020). TTVs can also be used to constrain the masses of the planets involved (see for example Nesvorný et al. 2013), hence their density, which ultimately give constraints on their internal structures, as is the case for the Trappist-1 system (Grimm et al. 2018; Agol et al. 2020). Detection of individual dynamically active systems

also provides valuable constraints on planetary system formation theory, as the current orbital state of a system can display markers of its evolution (see for example Batygin & Morbidelli 2013; Delisle 2017). Orbital interactions also impact the possible rotation state of the planets (Delisle et al. 2017), hence their atmosphere (Lecante et al. 2015).

However, TTVs can also be a bias that affects negatively the detection and characterisation of exoplanets. As previously stated, transit surveys rely on stacking the lightcurve over constant period to extract the shallow transits from the noise. If TTVs of amplitude comparable to - or greater than - the duration of the transit occur on a timescale comparable to - or shorter than - the mission duration, there is not a unique period that will successfully stack the transits of the planet (García-Melendo & López-Morales 2011). This can lead to two problems: incorrect estimates of the planet parameters, and/or the absence of detection. To alleviate this bias, we developed the RIVERS method, based on the recognition of the tracks of planets in river diagrams using machine learning, and a photo-dynamic fit of the lightcurve. The method is described in details in Leleu et al. (2021b).

In this paper we apply the RIVERS method to KIC 4725681, which have 3 KOIs announced on the Kepler database¹, the candidates KOI3184.01 and .03 with orbital periods of 7.54 and 4.02 days, respectively, and the False-positive KOI3184.02 at a period of 11.32 day, flagged as 'Not transit-like'.

2. Detection of Kepler-1972

2.1. Application of the RIVERS.deep method

2.1.1. Preparation of the lightcurve

The raw PDCSAP flux is downloaded using the `lightkurve`² package. We started by removing long-term trends of the flux using the `flatten`³ method of the `lightkurve` package using the default parameters. This method apply a Savitzky-Golay filter on the lightcurve. We then checked for gaps longer than 2.5 hours. Such gaps were commonly produced by the monthly data downlinks. After repointing the spacecraft, there was usually a photometric offset produced due to thermal changes in the telescope. We hence removed all data points until the average flux over 4 hours is within 1 standard deviation of the median flux of the lightcurve. Finally, we removed points at more that 4 times the standard deviation from the median value of the lightcurve to remove outliers.

2.1.2. Application of RIVERS.deep

The RIVERS.deep method, introduced in details in Leleu et al. (2021b), is based on the recognition of the track of a planet in a river diagram (Carter et al. 2012). An example of such diagram is given on the top panel of Fig. 1. The RIVERS.deep algorithm takes as input this 2D array and produces two outputs:

- **a confidence matrix:** an array of the same size as the input containing for each pixel the confidence that

this pixel belongs to a transit. This task is performed by the 'semantic segmentation' (pixel-level vetting) sub-network (Jégou et al. 2017).

- **a global prediction:** a value between 0 and 1 which quantifies the model confidence that the output of the semantic segmentation module is due to the presence of a planet. This task is performed by the classification subnetwork.

An example of confidence matrix is shown on the bottom panel of Fig. 1. The pixels recognized as belonging to a transit are highlighted in yellow. As described in section 3.2.3 of Leleu et al. (2021b), a periodogram can be obtained by saving the output of the global prediction of the model over a series of river diagrams, made for a grid of folding periods. The RIVERS.deep periodogram of KIC 4735826 is displayed in Fig. 2. This periodogram shows two strong peaks at 7.5d and 11.3d. One of the river diagram belonging to the 7.5d (resp. 11.3d) peak is the top-left (resp. top-right) diagram in Fig. 1. The transit timings proxy highlighted in the bottom panels of Fig. 1 are recovered and displayed as black data points in Fig. 3. We emphasise that the word 'confidence' used here refer to the output of a neural network, which is not a likelihood or probability. As such, the application of RIVERS.deep is only a preliminary step to the photo dynamical fit of the lightcurve presented in the next section.

2.2. Planet detection

2.2.1. Stellar properties

The luminosity of KIC 4735826 is computed from the *Gaia* Early Data Release 3 parallax (Gaia Collaboration et al. 2021) by taking into account the correction to the parallax from Lindegren et al. (2021). The K magnitude of the star is used together with the bolometric correction of Casagrande & Vandenberg (2014, 2018) and the extinction from the dust map of Green et al. (2018). We then obtain a luminosity $L = 1.97 \pm 0.07 L_{\odot}$ for KIC 4735826. The effective temperature and metallicity of KIC 4735826 are taken from the spectroscopic analysis of Brewer & Fischer (2018): $T_{\text{eff}} = 5818 \pm 27$ K and $[M/H] = 0.23 \pm 0.01$ dex.

These observational constraints (L , T_{eff} and $[M/H]$) are then used to determine the global parameters of KIC 4735826 from stellar models computed with the Geneva stellar evolution code (Eggenberger et al. 2008). For this determination, the adopted uncertainty on the effective temperature was increased to 50 K (instead of the small internal error of 27 K) to better account for possible uncertainties coming from different spectroscopic determinations. We then find that KIC 4735826 is a star at the end of its evolution on the main sequence with a mass of $M = 1.12 \pm 0.03 M_{\odot}$, a radius of $R = 1.384 \pm 0.050 R_{\odot}$ and an age of 7.4 ± 1.2 Gyr. The stellar properties are summarized in Table 1.

2.2.2. Planetary solution

The fit of the lightcurve was performed with the same setup as the one presented in Leleu et al. (2021b). To highlight the effect of the TTVs on the recovered transit parameters, we performed two distinct fits of the lightcurve: a fit with `KeplerianOrbits` (constant periods) for the three candidates

¹ <https://exoplanetarchive.ipac.caltech.edu/cgi-bin/TblView/nph-tblView?app=ExoTbls&config=cumulative>

² <https://docs.lightkurve.org/>

³ <https://docs.lightkurve.org/reference/api/lightkurve.LightCurveKeplerianOrbits>

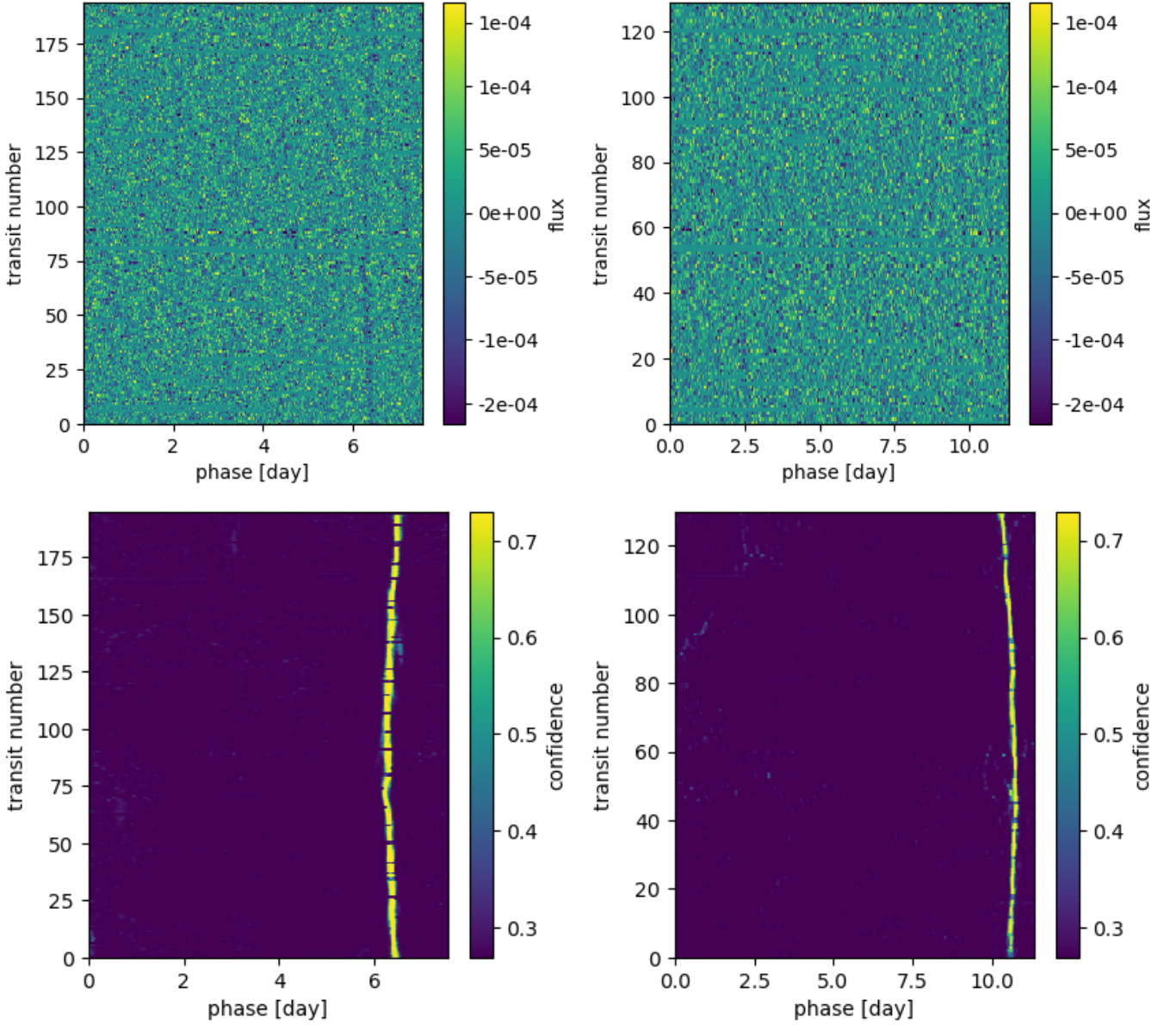


Fig. 1: *Top*: Rivers diagrams of KOI3184 at the period 7.5472d (*left*) and 11.3251d (*right*). The bottom row displays the first 7.5472 (resp. 11.3251) days of data for KOI3184, the color code representing the normalised flux. Each subsequent raw display a new set of 7.5472 (resp. 11.3251) days of data. The flux has been clipped at 3σ for visibility, and missing data have been replaced by a flux of 1. *Bottom*: corresponding RIVERS.deep confidence matrices, which shows for each timing of the rivers diagram the confidence for it to belong to the track of a planet. See section 2.1.2 for more details about the confidence matrix.

at 4, 7.5, and 11.3 days, and a photodynamic fit where the transit timings of the two resonant planets were modelled using the TTVfast algorithm (Deck et al. 2014). The approximate initial conditions for the orbital elements and masses of these planets were obtained by a preliminary fit of the transit timings to the timing proxy shown in Fig. 3. In the photodynamic fit, the orbit of the 4d candidate is still considered as Keplerian since its interactions with the other two planets are negligible over the duration of the Kepler mission.

For both fits, we use the adaptive MCMC sampler `samsam`⁴ (see Delisle et al. 2018), which learns the covariance of the target distribution from previous samples in order to improve the subsequent sampling efficiency. The likelihood is defined as :

$$\begin{aligned} \ln \mathcal{L}(\theta, \alpha) &= \ln p(y|\theta, \alpha) \\ &= -\frac{1}{2} (y - m(\theta))^T C^{-1}(\alpha) (y - m(\theta)) \\ &\quad - \frac{1}{2} \ln \det (2\pi C(\alpha)) \end{aligned} \quad (1)$$

⁴ <https://gitlab.unige.ch/Jean-Baptiste.Delisle/samsam>

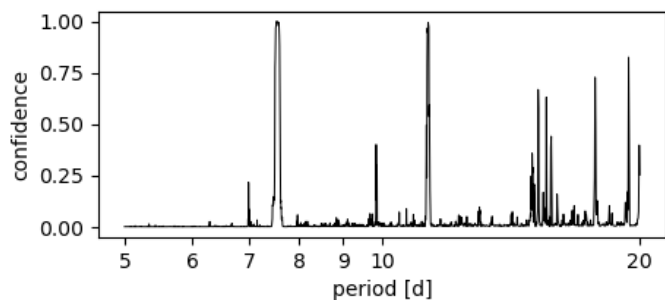


Fig. 2: RIVERS periodogram of KIC 4735826: For each period we show the confidence of the RIVERS.deep classifier that the corresponding river diagram contain the track of a planet. Since the false positive rate of the classifier is typically of a few percent, a photo dynamical fit of the data is required to confirm the planetary nature of the signals.

Table 1: Stellar global properties of Kepler-1972. The upper panel provides the adopted observational constraints used to determine the global stellar properties from stellar models given in the lower panel of the Table.

Kepler-1972		
KIC	4735826	
Parameter	Value	Reference
mKep [mag]	11.158	1
mV [mag]	11.230 ± 0.034	1
mJ [mag]	10.118 ± 0.021	1
mH [mag]	9.858 ± 0.020	1
T_{eff} [K]	5818 ± 27	2
[M/H] [dex]	0.23 ± 0.01	2
L_{\star} [L_{\odot}]	1.97 ± 0.07	3
M_{\star} [M_{\odot}]	1.12 ± 0.03	3
R_{\star} [R_{\odot}]	1.384 ± 0.050	3
t_{\star} [Gyr]	7.4 ± 1.2	3
$\log g$ [cgs]	4.20 ± 0.04	3
ρ_{\star} [ρ_{\odot}]	0.422 ± 0.050	3

Notes. [1] <https://exoplanetarchive.ipac.caltech.edu> [2] Brewer & Fischer (2018), [3] this study

where y is the photometric data and θ is the vector of the fitted planetary parameters given in table 2 as well as the limb-darkening coefficients and stellar density. The lightcurve model $m(\theta)$ was obtained by computing the transit timings for the chosen type of orbit (Keplerian ephemerides or n-body), then by modeling the transits of each planet with the `batman` package (Kreidberg 2015), with a supersampling parameter set to 29.42 minutes to account for the long exposure of the dataset. The effective temperature, $\log g$ and metallicity of the star (Table 1) were used to compute the quadratic limb-darkening coefficients u_1 and u_2 and their error-bars adapted to the Kepler spacecraft using LDCU⁵. Based on the `limb-darkening` package (Espinoza & Jordán 2015), LDCU uses two libraries of stellar atmosphere models ATLAS9 (Kurucz 1979) and PHOENIX (Husser et al. 2013) to compute stellar intensity profiles for a given pass-band. Remaining long-term trends were modeled using the S+LEAF (Delisle et al. 2020).

⁵ <https://github.com/delinea/LDCU>

S+LEAF is a C library with python wrappers that implements an optimized GP framework. While the computational cost of classical GP implementations typically scales has the cube of the dataset size, the cost of a S+LEAF GP scales linearly (Foreman-Mackey et al. 2017; Delisle et al. 2020, 2022). We used a gaussian process framework with a Matérn 3/2 kernel whose timescale was forced to be above one day (uniform prior of the log of the timescale τ_{GP} set to $U[0, 3]$) to avoid interfering with the modeled transits. A jitter term was also added to all photometric measurements. α is the vector of the noise parameters (jitter, σ_{GP} , τ_{GP}). $C(\alpha)$ is the corresponding covariance matrix.

The posterior of the fits are summarised in Table 2, with the Keplerian model on the left and the n-body model on the right. The recovered stacked transits are shown on Fig. 4. The difference in the models for the two outer candidates did not affect much the fit of the inner candidate, for which the fit converged to a radius of $0.551^{+0.034}_{-0.034} R_{\text{Earth}}$. The difference is significant for the two resonant planets : the transits stacked along a Keplerian ephemerides yield a strong dispersion of points in and near-transit, responsible for the false positive flag attributed to KOI3184.02 by the Kepler pipeline. Stacking the transits along the TTV-corrected transit timings greatly reduce the in-transit scattering, as can be seen in the right-hand side of Fig. 4. The photodynamic fit yields radius of $0.802^{+0.042}_{-0.041}$ and $0.868^{+0.051}_{-0.050} R_{\text{Earth}}$ for Kepler-1972 b and c, respectively, while the Keplerian model yields radii smaller by $\sim 28\%$ and $\sim 35\%$, respectively. Finally, the photodynamic fit yields projected inclinations of $87.25^{+1.31}_{-0.97}$, $87.62^{+0.73}_{-0.49}$ and $87.13^{+0.17}_{-0.19}$, which are consistent with a coplanar system.

The estimated masses are of $2.02^{+0.56}_{-0.62}$ and $2.11^{+0.59}_{-0.65} M_{\text{Earth}}$ for Kepler-1972 b and c, respectively, resulting in densities of $4.02^{+1.44}_{-1.31}$ and $3.33^{+1.17}_{-1.07} \rho_{\text{Earth}}$. Although the densities are poorly constrained, the planets appear to be denser than the Earth. The mass distribution between the two planets is well constrained $m_{01}/(m_{01} + m_{02}) = 0.489^{+0.014}_{-0.013}$, while the total mass of the planets is not. This is due to the TTV signal dependency on the parameters: the mass distribution is linked to the relative amplitude of the TTVs between the two planets, while the total planetary mass is constrained by the TTV period (Agol et al. 2005; Nesvorný & Vokrouhlický 2016). The latter could not be properly estimated with the available baseline: as can be seen on the posterior of the TTVs shown in Fig. 3, there is a range of TTV periods that are consistent with the observed signal.

3. The resonant pair of Kepler-1972

In this section we study a sub-population of 2300 randomly-chosen samples from the posteriors presented in Table 2. Fig. 5 shows the projection of these samples in the $(\sqrt{e_1^2 + c^2 e_2^2}, \Delta\varpi = \varpi_2 - \varpi_1)$ plane ($c = -1.22$ for the 3:2 MMR and is discussed in section 5.2 of Leleu et al. 2021b). The e_j and ϖ_j represented here are the fitted initial conditions at the date 2454943.5394 BJD.

3.1. Stability

We verified the stability of the posteriors using the frequency analysis criterion (Laskar 1990, 1993), using the

Table 2: Fitted and derived properties of the planets and candidate of the Kepler-1972 system

Parameter	Prior	Keplerian	n-body	
KOI3184.03				
P [day]	U[8,12]	$4.020192^{+3.5e-05}_{-3.4e-05}$	$4.020184^{+3.6e-05}_{-3.5e-05}$	fitted
R/R_*	U[0,1e-1]	$0.00372^{+1.9e-04}_{-1.9e-04}$	$0.00365^{+1.8e-04}_{-1.8e-04}$	fitted
b	U[0,1]	$0.51^{+0.08}_{-0.11}$	$0.39^{+0.13}_{-0.18}$	fitted
t_0 [BJD-2454833.0]		$134.8402^{+0.0083}_{-0.0080}$	$134.8424^{+0.0082}_{-0.0082}$	fitted
a/R_*		$7.98^{+0.30}_{-0.32}$	$8.11^{+0.27}_{-0.29}$	derived
I [deg]		$86.35^{+0.77}_{-0.58}$	$87.25^{+1.31}_{-0.97}$	derived
R [R_{Earth}]		$0.561^{+0.035}_{-0.035}$	$0.551^{+0.034}_{-0.034}$	derived
SNR		11.14	11.10	derived
Kepler-1972 b (KOI3184.01)				
λ [deg]	U[0,360]	–	$23.46^{+4.79}_{-4.72}$	fitted
P [day]	U[1,20]	$7.54765^{+1.2e-04}_{-1.3e-04}$	$7.54425^{+5.4e-04}_{-5.4e-04}$	fitted
$e \cos \varpi$	U[-.9,.9]*	–	$0.014^{+0.045}_{-0.043}$	fitted
$e \sin \varpi$	U[-.9,.9]*	–	$0.045^{+0.060}_{-0.044}$	fitted
M_{pl}/M_*	U[0,1e-2]	–	$5.4e-06^{+1.5e-06}_{-1.7e-06}$	derived
R_{pl}/R_*	U[0,1e-1]	$0.00391^{+1.6e-04}_{-1.6e-04}$	$0.00532^{+2.0e-04}_{-1.9e-04}$	fitted
b	U[0,1]	$0.13^{+0.13}_{-0.09}$	$0.51^{+0.09}_{-0.15}$	fitted
t_0 [BJD-2454833.0]		$134.406^{+0.016}_{-0.013}$	$111.8999^{+0.0078}_{-0.0090}$	f/d
a/R_*		$12.15^{+0.45}_{-0.49}$	$12.34^{+0.41}_{-0.44}$	derived
e		–	$0.067^{+0.071}_{-0.040}$	derived
ϖ [deg]		–	$64.9^{+50.1}_{-57.2}$	derived
I [deg]		$89.05^{+0.67}_{-0.94}$	$87.62^{+0.73}_{-0.49}$	derived
M_{pl} [M_{Earth}]		–	$2.02^{+0.56}_{-0.62}$	derived
R_{pl} [R_{Earth}]		$0.590^{+0.032}_{-0.033}$	$0.802^{+0.042}_{-0.041}$	derived
ρ_{pl} [ρ_{Earth}]		–	$4.02^{+1.44}_{-1.31}$	derived
SNR		12.38	18.96	derived
Kepler-1972 c (KOI3184.02)				
λ [deg]	U[0,360]	–	$156.60^{+4.06}_{-3.57}$	fitted
P [day]	U[1,20]	$11.32057^{+2.8e-04}_{-2.5e-04}$	$11.3295^{+0.0011}_{-0.0011}$	fitted
$e \cos \varpi$	U[-.9,.9]*	–	$-0.007^{+0.037}_{-0.037}$	fitted
$e \sin \varpi$	U[-.9,.9]*	–	$-9.6e-04^{+0.046}_{-0.036}$	fitted
M_{pl}/M_*	U[0,1e-2]	–	$5.7e-06^{+1.6e-06}_{-1.7e-06}$	derived
R_{pl}/R_*	U[0,1e-1]	$0.00398^{+3.2e-04}_{-3.3e-04}$	$0.00575^{+2.6e-04}_{-2.6e-04}$	fitted
b	U[0,1]	$0.68^{+0.07}_{-0.11}$	$0.810^{+0.033}_{-0.031}$	fitted
t_0 [BJD-2454833.0]		$142.839^{+0.019}_{-0.020}$	$119.800^{+0.014}_{-0.012}$	f/d
a/R_*		$15.91^{+0.59}_{-0.64}$	$16.19^{+0.54}_{-0.58}$	derived
e		–	$0.043^{+0.046}_{-0.028}$	derived
ϖ [deg]		–	-10^{+139}_{-119}	derived
I [deg]		$85.13^{+0.80}_{-0.58}$	$87.13^{+0.17}_{-0.19}$	derived
M_{pl} [M_{Earth}]		–	$2.11^{+0.59}_{-0.65}$	derived
R_{pl} [R_{Earth}]		$0.601^{+0.054}_{-0.055}$	$0.868^{+0.051}_{-0.050}$	derived
ρ_{pl} [ρ_{Earth}]		–	$3.33^{+1.17}_{-1.07}$	derived
SNR		7.47	12.60	derived
Kepler-1972 b and c				
$\log_{10}((m_b + m_c)/m_*)$	U[-7,-2]	–	$-4.96^{+0.11}_{-0.16}$	fitted
$m_b/(m_b + m_c)$	U[0,1]	–	$0.489^{+0.014}_{-0.014}$	fitted
Kepler-1972				
ρ_* [ρ_\odot]	$\mathcal{N}(0.422,0.050)$	$0.423^{+0.049}_{-0.049}$	$0.444^{+0.046}_{-0.046}$	fitted
limbdark u_1	$\mathcal{N}(0.454,0.026)$	$0.455^{+0.026}_{-0.026}$	$0.454^{+0.025}_{-0.025}$	fitted
limbdark u_2	$\mathcal{N}(0.236,0.036)$	$0.237^{+0.036}_{-0.036}$	$0.237^{+0.035}_{-0.036}$	fitted
$\log_{10}(\text{jitter})$	U[-10,0]	$-4.3931^{+0.0022}_{-0.0022}$	$-4.3951^{+0.0022}_{-0.0022}$	fitted
$\log_{10}(\sigma_{GP})$	U[-10,0]	$-8.27^{+1.16}_{-1.16}$	$-8.24^{+1.10}_{-1.16}$	fitted
$\log_{10}(\tau_{GP})$ [day]	U[0,3]	$1.50^{+1.01}_{-1.02}$	$1.51^{+1.00}_{-1.00}$	fitted

Notes. Orbital elements are given at the date 110.5394 [BJD-2454833.0]. The main value is the median of the posterior distribution. The reported errors are the distance to the 0.15865 quantile (lower error) and 0.84135 quantile (upper error). U refer to a flat prior between the given bounds, while $\mathcal{N}(\mu, \sigma)$ refer to a gaussian distribution of mean μ and standard deviation σ . U*: For the $k = e \cos \varpi$ and $h = e \sin \varpi$ variables, an additional prior was added to enforce an uniform distribution for their module e . f/d indicates that the variable is fitted for the circular model, but derived in the n-body model (where λ_j is the fitted parameter). The reported SNR is the median depth of transit over its standard deviation to better account for potential degeneracy with the noise modelling at the transit location.

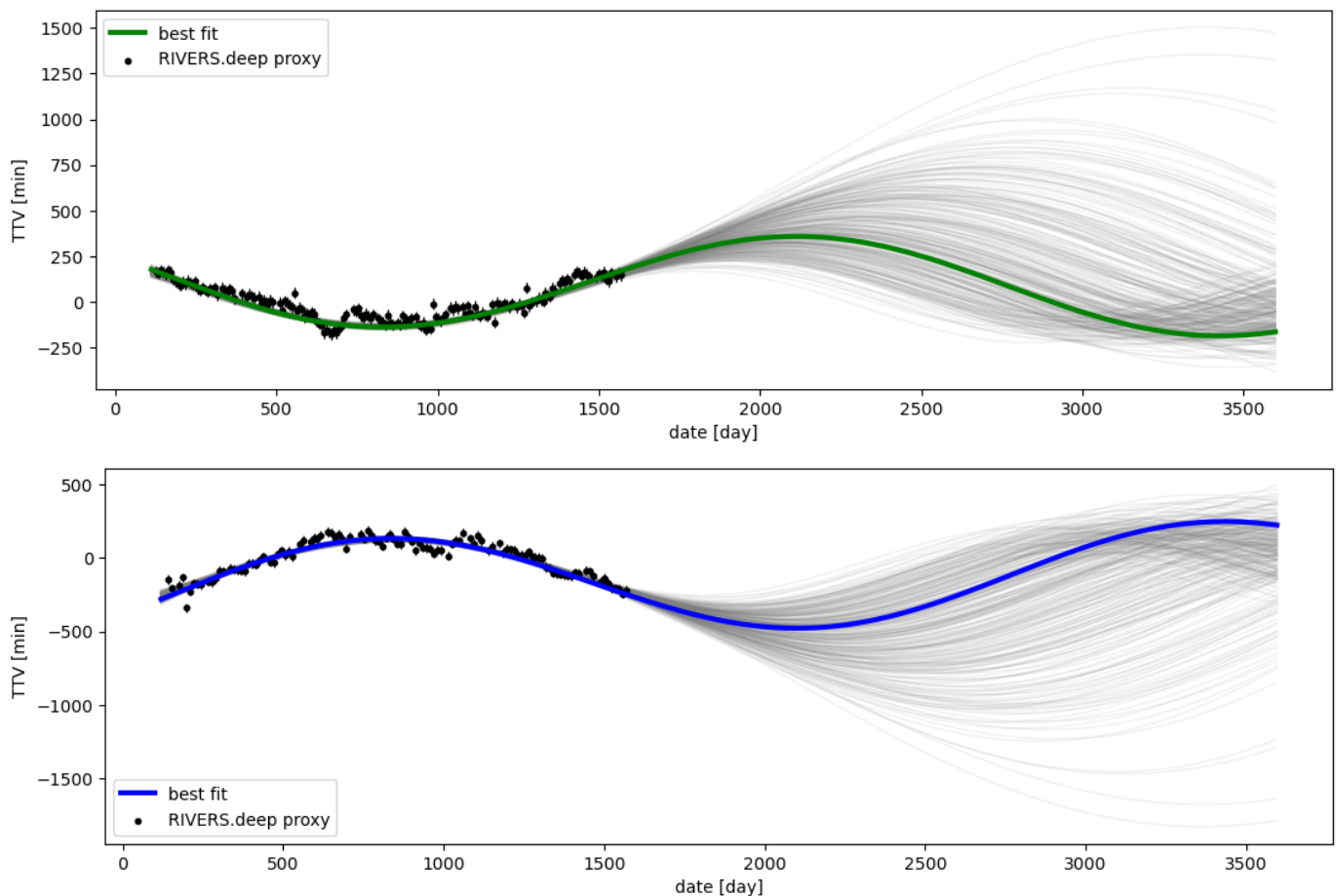


Fig. 3: TTVs for Kepler-172 b (*top*) and Kepler-172 c (*bottom*). The black errorbars represent the TTVs coming from the RIVERS.deep method which is the network’s highest confidence for the timing of each transit (highlighted pixels in Fig. 1). These timings are used as TTV proxy to initialise the photodynamical fit close to its final solution, but are not transit timings fitted to the data. Their errorbar indicate the sensitivity of the method (30 min). In grey are 300 samples resulting from the photodynamic fit of the lightcurve, the solid coloured curves correspond to the best fit.

same implementation as in Leleu et al. (2021a,b). For this stability analysis, the resonant pair and the inner candidate at 4.02 d were considered. Since only the radius of this inner candidate could be derived in our analysis, we assumed its density to be of $2.6\rho_{Earth}$, an arbitrary value which is consistent with the densities of the two outer planets. The top panel of Fig. 5 shows the resulting criterion for each initial condition, for n-body integration over 10^5 years. We find that the bulk of the low-eccentricity part of the posterior is stable for more than 10^6 year, which together correspond to more than 45 billion orbits of the resonant pair. On the other hand, a significant part of the posterior is unstable on a short time-scale (red dots on the top panel of Fig. 5) for eccentricities typically higher than ~ 0.1 .

3.2. Dynamics and TTV degeneracy

3.2.1. Resonant state of the system

We consider the Hamiltonian formulation of the Second Fundamental Model for Resonance of (Henrard & Lemaître 1983). Using the 1-degree of freedom model of first order resonances presented in Deck et al. (2013), the dynamics of a resonant system can be derived from the equations canon-

ically associated with the conjugated variables X and Y of the Hamiltonian:

$$H = \frac{1}{2} \left[\frac{1}{2} (X^2 + Y^2) - \Gamma' \right]^2 - X \quad (2)$$

The change of coordinates from the orbital elements and masses to the variables X and Y are given in section 2 of Deck et al. (2013). For $\Gamma' < 1.5$ the model has a single family of elliptic fixed points and no separatrix. At $\Gamma' = 1.5$ a bifurcation occurs and for $\Gamma' > 1.5$ there are two families of elliptic fix points and one family of hyperbolic fix points from which emanates a separatrix. Systems are considered formally resonant when $\Gamma' > 1.5$ and they lie inside the separatrix. Since $Y = 0$ for all fixed points, and all trajectories of the Hamiltonian 2 cross the $Y = 0$ line, we show a surface of section of the Hamiltonian for $Y = 0$ in Fig. 6. This representation is equivalent to the one presented in Nesvorný & Vokrouhlický (2016); Nesvorný et al. (2021). The blue dots represent the posterior of Kepler-172, while the orange dots show the position of Kepler-1705, for comparison. Despite the large uncertainties on the orbital parameters and masses due to the observation baseline shorter than the resonant period, the whole posterior lies inside the 3:2 MMR.

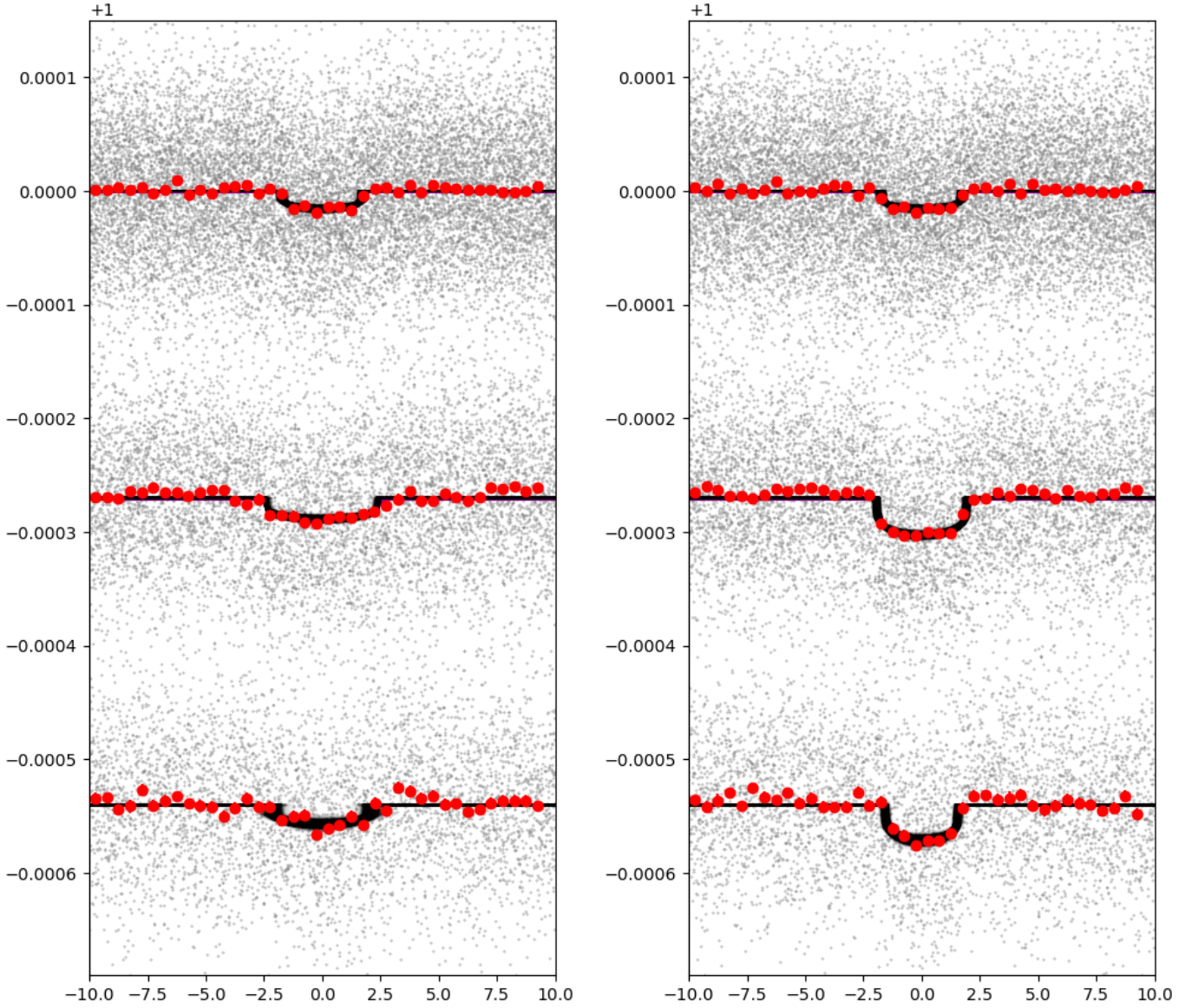


Fig. 4: Stacked transits of KOI3184.03 (*top*), Kepler-1972 b (*middle*), and Kepler-1972 c (*bottom*). The left panel results from the stacking along the Keplerian ephemeride, which is the left solution in table 2. The right panel result from the stacking along the Keplerian ephemeride, for the inner planet, and the n-body solution for Kepler-1972 b and c, which is the right solution in table 2

3.2.2. TTV degeneracy

In Leleu et al. (2021b) we introduced the variables

$$u = e_b e^{i\phi_1} + c e_c e^{i\phi_2} \quad \text{and} \quad v = c e_b e^{i\phi_1} - g e_c e^{i\phi_2} \quad (3)$$

(Mardling, in prep), where

$$\phi_1 = 2\lambda_b - 3\lambda_c + \varpi_b \quad \text{and} \quad \phi_2 = 2\lambda_b - 3\lambda_c + \varpi_c \quad (4)$$

are the resonant angles for the 3:2 resonance, c is a function of the Laplace coefficients whose value is -1.23 for the 3:2 commensurability, and $g = (m_2/m_1)\sqrt{a_2/a_1}$. For Kepler-1705 (the system discovered in Leleu et al. 2021b), a full resonant period is observed, and as a result Γ' (and the corresponding range of values of u) is well determined and varies little across the posterior. In that case, we showed

that the theoretical posterior of the variables e_j and ϖ_j could be obtained by varying the real and imaginary parts of v in the range $[-0.2, 0.2]$; indeed, the TTV signal constrains the resonant part of the eccentricity u , but is blind to the free part v (Mardling, in prep, Leleu et al. 2021b). In Kepler-1972 however, Γ' (and u) is poorly constrained across the posterior, which parametrizes an additional degeneracy for the e_j and ϖ_j variables; see the middle panel of Fig.5.

4. Summary and Conclusion

For planets that are too small to induce individually-detectable transits, the shape of their transit is derived from light curves that are stacked along constant periods. In this case, TTVs can lead to erroneous estimations of the tran-

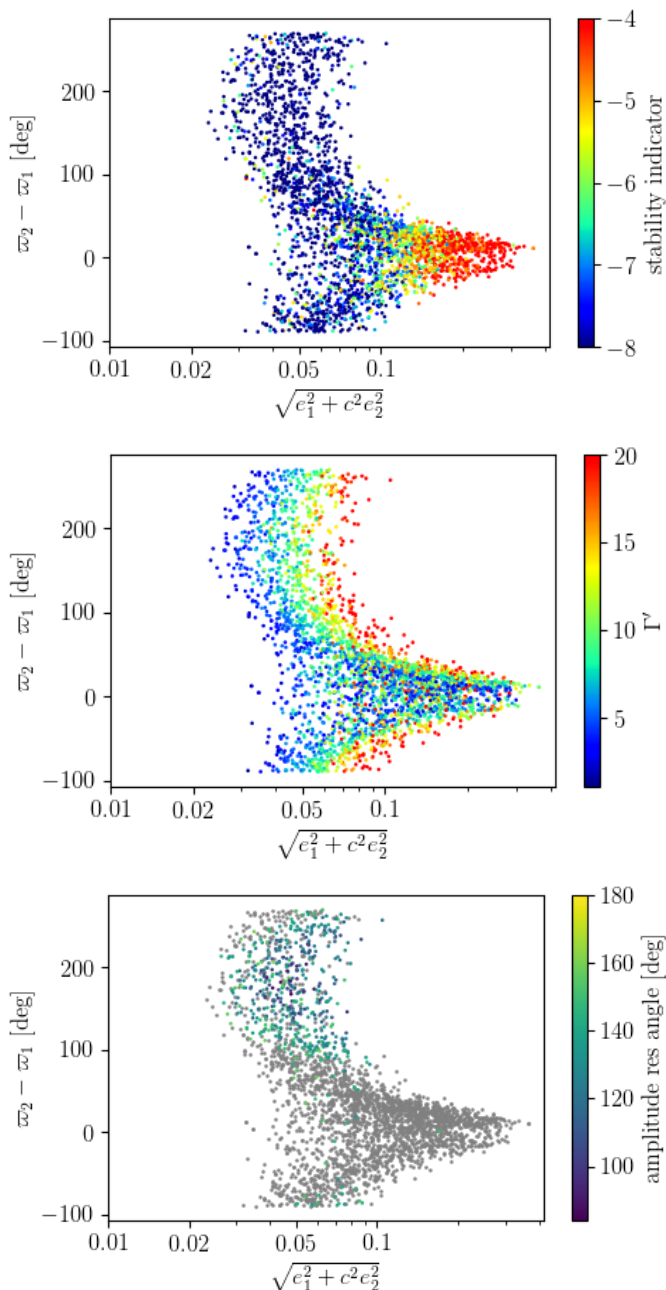


Fig. 5: Posterior of the solution shown in Table 2. The $c = -1.22$ parameter is discussed in (Leleu et al. 2021b). *Top*: stability of the posteriors, ranging from stable (blue) to unstable (red). *Middle*: Value of the Hamiltonian parameter Γ' over the posterior. *Bottom*: Smallest amplitude between the two resonant angles. Grey dots indicate a circulation of both of them.

sit depth and duration, or even create a signal that is not recognised as a transit anymore. We illustrate this on KOI-3184.02, which is flagged as ‘Not transit-like false positive’ on the NASA Exoplanet Archive as of November 2021. Applying the RIVERS methods, we retrieved the track of KOI-3184.01 and KOI-3184.02 in the lightcurve. We show that both of these planets have anti-correlated TTVs of 6 hour of peak-to-peak amplitude, these TTVs being responsible for

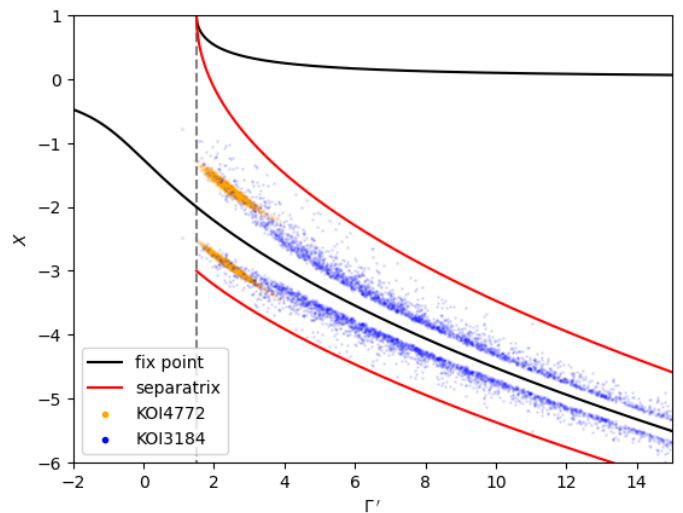


Fig. 6: Surface of section in the (Γ', X) plane of the Hamiltonian (2). The black line shows the positions of the family of elliptic fixed point (the hyperbolic family exist for larger value of X and is not displayed here). The red line show the intersection of the separatrix with the $Y = 0$ plane for each value of Γ' . The coloured dots show the intersection of the trajectories emanating from the initial conditions of the posterior summarised in section 2 and the (Γ', X) plane, for Kepler-1772 (this paper) and Kepler-1705 (Leleu et al. 2021b)

the apparent incoherence of their transit signature. We now name these planets Kepler-1772 b and c. As for Kepler-1705 (Leleu et al. 2021b), the recovered planets have individual transit SNR of ~ 1 , showcasing the performance of the approach to recover individual transits that would otherwise be lost in the noise.

Kepler-1772 b and c is a pair of Earth-sized planets with $R_b = 0.802^{+0.042}_{-0.041} R_{Earth}$ and $R_c = 0.868^{+0.051}_{-0.050} R_{Earth}$, with similar masses $m_b/m_c = 0.956^{+0.056}_{-0.051}$. The observed TTV signal is enough to show that the pair is formally inside the 3:2 mean motion resonance (inside the separatrix). However, the baseline of the observation is not long enough to cover a full period of the TTV signal, leading to a somewhat imprecise estimation of the planet masses, putting an 1σ upper limit at $M_b = 2.58 M_{Earth}$ and $M_c = 2.70 M_{Earth}$. Fitting the inner candidate (KOI-3184.03, $P = 4.02[\text{day}]$) at the same time as the resonant pair, we show that the three projected inclinations are 1σ compatible: $I_{03} = 87.25^{+1.31}_{-0.97}$, $I_b = 87.62^{+0.73}_{-0.49}$, and $I_c = 87.13^{+0.17}_{-0.19}$ degrees. This is consistent with a co-planar 3-planet system, which increases the probability that the 4.02d signal is also of planetary nature.

Recovering a planetary signal from a Kepler false positive shows that special care needs to be taken in the treatment of low-S/R planet candidates in transit surveys, as the stacking methods broadly used is not well suited when planet-planet interactions induce TTVs larger than the transit duration. This effect is especially relevant for the Kepler mission, TESS polar observations, and the upcoming PLATO mission.

Acknowledgements. This work has been carried out within the framework of the National Centre of Competence in Research PlanetS supported by the Swiss National Science Foundation and benefited from the seed-funding program of the Technology Platform of PlanetS. The authors acknowledge the financial support of the SNSF.

References

- Agol, E. & Deck, K. 2016, *ApJ*, 818, 177
- Agol, E., Dorn, C., Grimm, S. L., et al. 2020, arXiv e-prints, arXiv:2010.01074
- Agol, E., Steffen, J., Sari, R., & Clarkson, W. 2005, *MNRAS*, 359, 567
- Alibert, Y., Carron, F., Fortier, A., et al. 2013, *A&A*, 558, A109
- Batygin, K. & Morbidelli, A. 2013, *Astron. Astrophys.*, 556, A28
- Brewer, J. M. & Fischer, D. A. 2018, *ApJS*, 237, 38
- Carter, J. A., Agol, E., Chaplin, W. J., et al. 2012, *Science*, 337, 556
- Casagrande, L. & VandenBerg, D. A. 2014, *MNRAS*, 444, 392
- Casagrande, L. & VandenBerg, D. A. 2018, *MNRAS*, 475, 5023
- Coleman, G. A. L., Leleu, A., Alibert, Y., & Benz, W. 2019, *A&A*, 631, A7
- Deck, K. M., Agol, E., Holman, M. J., & Nesvorný, D. 2014, *ApJ*, 787, 132
- Deck, K. M., Payne, M., & Holman, M. J. 2013, *ApJ*, 774, 129
- Delisle, J. B. 2017, *A&A*, 605, A96
- Delisle, J.-B., Correia, A. C. M., Leleu, A., & Robutel, P. 2017, *aap*, 605, A37
- Delisle, J. B., Hara, N., & Ségransan, D. 2020, *A&A*, 638, A95
- Delisle, J. B., Ségransan, D., Dumusque, X., et al. 2018, *A&A*, 614, A133
- Delisle, J. B., Unger, N., Hara, N. C., & Ségransan, D. 2022, arXiv e-prints, arXiv:2201.02440
- Dobrovolskis, A. R. & Borucki, W. J. 1996, in *BAAS*, Vol. 28, 1112
- Eggenberger, P., Meynet, G., Maeder, A., et al. 2008, *Ap&SS*, 316, 43
- Emsenhuber, A., Mordasini, C., Burn, R., et al. 2020, arXiv e-prints, arXiv:2007.05561
- Espinoza, N. & Jordán, A. 2015, *MNRAS*, 450, 1879
- Foreman-Mackey, D., Agol, E., Ambikasaran, S., & Angus, R. 2017, *AJ*, 154, 220
- Gaia Collaboration, Brown, A. G. A., Vallenari, A., et al. 2021, *A&A*, 649, A1
- García-Melendo, E. & López-Morales, M. 2011, *MNRAS*, 417, L16
- Green, G. M., Schlafly, E. F., Finkbeiner, D., et al. 2018, *MNRAS*, 478, 651
- Grimm, S. L., Demory, B.-O., Gillon, M., et al. 2018, *A&A*, 613, A68
- Henrard, J. & Lemaitre, A. 1983, *Celestial Mechanics*, 30, 197
- Holczer, T., Mazeh, T., Nachmani, G., et al. 2016, *ApJS*, 225, 9
- Husser, T. O., Wende-von Berg, S., Dreizler, S., et al. 2013, *A&A*, 553, A6
- Jégou, S., Drozdal, M., Vazquez, D., Romero, A., & Bengio, Y. 2017, in *Proceedings of the IEEE conference on computer vision and pattern recognition workshops*, 11–19
- Jenkins, J. M., Caldwell, D. A., Chandrasekaran, H., et al. 2010, *ApJ*, 713, L87
- Jenkins, J. M., Twicken, J. D., McCauliff, S., et al. 2016, in *Proc. SPIE*, Vol. 9913, *Software and Cyberinfrastructure for Astronomy IV*, 99133E, tESS SPOC pipeline
- Kane, M., Ragozzine, D., Flowers, X., et al. 2019, *AJ*, 157, 171
- Kovács, G., Zucker, S., & Mazeh, T. 2002, *A&A*, 391, 369
- Kreidberg, L. 2015, *PASP*, 127, 1161
- Kurucz, R. L. 1979, *ApJS*, 40, 1
- Laskar, J. 1990, *Icarus*, 88, 266
- Laskar, J. 1993, *Phys. D*, 67, 257
- Leconte, J., Wu, H., Menou, K., & Murray, N. 2015, *Science*, 347, 632
- Leleu, A., Alibert, Y., Hara, N. C., et al. 2021a, *A&A*, 649, A26
- Leleu, A., Chatel, G., Udry, S., et al. 2021b, *A&A*, 655, A66
- Lindegren, L., Bastian, U., Biermann, M., et al. 2021, *A&A*, 649, A4
- Lithwick, Y., Xie, J., & Wu, Y. 2012, *ApJ*, 761, 122
- Mazeh, T., Nachmani, G., Holczer, T., et al. 2013, *ApJS*, 208, 16
- Mordasini, C. 2018, *Planetary Population Synthesis*, 143
- Mordasini, C., Alibert, Y., Benz, W., & Naef, D. 2009, *A&A*, 501, 1161
- Nesvorný, D., Chrenko, O., & Flock, M. 2021, arXiv e-prints, arXiv:2110.09577
- Nesvorný, D., Kipping, D., Terrell, D., et al. 2013, *ApJ*, 777, 3
- Nesvorný, D. & Vokrouhlický, D. 2014, *apj*, 790, 58
- Nesvorný, D. & Vokrouhlický, D. 2016, *ApJ*, 823, 72
- Rowe, J. F. & Thompson, S. E. 2015, arXiv e-prints, arXiv:1504.00707
- Xie, J.-W., Wu, Y., & Lithwick, Y. 2014, *ApJ*, 789, 165
- Zhu, W., Petrovich, C., Wu, Y., Dong, S., & Xie, J. 2018, *ApJ*, 860, 101